



Comparative study of multiwall carbon nanotube nanocomposites by Raman, SEM, and XPS measurement techniques

Yanmei Piao^{a,2}, Vipin N. Tondare^b, Chelsea S. Davis^{c,1,*}, Justin M. Gorham^d,
Elijah J. Petersen^e, Jeffrey W. Gilman^{c,3}, Keana Scott^d, András E. Vladár^f,
Angela R. Hight Walker^a

^a Nanoscale Device Characterization Division; Physical Measurement Laboratory, National Institute of Standards and Technology, Gaithersburg, MD, 20899, USA

^b Intelligent Systems Division, Engineering Laboratory National Institute of Standards and Technology, Gaithersburg, MD 20899, USA

^c Materials Science and Engineering Division; Materials Measurement Laboratory National Institute of Standards and Technology, Gaithersburg, MD, 20899, USA

^d Materials Measurement Science Division; Materials Measurement Laboratory National Institute of Standards and Technology, Gaithersburg, MD, 20899, USA

^e Biosystems and Biomaterials Division; Materials Measurement Laboratory National Institute of Standards and Technology, Gaithersburg, MD, 20899, USA

^f Microsystems and Nanotechnology Division; Physical Measurement Laboratory National Institute of Standards and Technology, Gaithersburg, MD, 20899, USA

ARTICLE INFO

Keywords:

Raman spectroscopy
Scanning electron microscopy (SEM)
Carbon nanotubes
Nanocomposites
Photoelectron spectroscopy (XPS)

ABSTRACT

Substantial research efforts are under way to optimize the production of composites enhanced by the incorporation of nanomaterial fillers such as multiwall carbon nanotubes (MWCNTs). It is therefore critical to develop robust methods to detect and characterize MWCNTs in nanocomposites to measure product performance and potential risks from release of the MWCNTs. In this study, the effectiveness of X-ray photoelectron spectroscopy (XPS), Raman spectroscopy, and scanning electron microscopy (SEM) methods is assessed on a series of MWCNT-epoxy nanocomposites samples. A general trend of positive correlation between signal intensity and MWCNT mass loading was observed by both Raman spectroscopy and XPS. Raman spectroscopy was capable of detecting MWCNTs at the lowest nominal concentration tested (0.01%), while for XPS, MWCNTs were detected down to a threshold of approximately 0.5%. Analysis of the same locations of two nanocomposite samples with nominal MWCNT mass fractions of 0.3% and 1% using Raman chemical imaging and SEM revealed a similar detectability of MWCNT clusters and with the higher mass loading sample having a greater number of MWCNT-rich domains. Overall, these results show a good comparability among the different techniques and therefore provide comprehensive, nondestructive microscopy methods to characterize nanocomposites.

1. Introduction

Nanocomposites (composites formed by the addition of nanomaterials to a polymer matrix) often have improved properties compared to the neat polymer, thereby yielding novel application opportunities[1]. Carbon nanotubes (CNTs), especially multiwall carbon nanotubes (MWCNTs), are a common nanomaterial filler in nanocomposites owing to exceptional properties such as their electrical/thermal conductivity, mechanical strength, and large surface area[2–9]. The improved properties of nanocomposites incorporating MWCNTs have led to research exploring their potential applications in a wide

range of industries such as construction and aerospace[10,11].

The substantial promise for nanocomposite materials in consumer products raises the importance of being able to accurately characterize MWCNTs in polymers. Developing methods to detect MWCNTs in nanocomposites can support research to optimize performance and to identify the potential risks to human health or the environment of MWCNT-enabled consumer products [12–14] as a possible result of MWCNT release during the product lifetime[15–23]. Numerous techniques have been established to detect and quantify loose MWCNTs in environmental and biological matrices[24–26]. However, there are very few protocols to characterize MWCNTs in nanocomposites and released

* Corresponding author.

E-mail address: chelsea@purdue.edu (C.S. Davis).

¹ Present Address: School of Materials Engineering, Purdue University, West Lafayette, IN 47907 USA.

² Present Address: Honeywell Aerospace, 3520 Westmoor St. South Bend, IN 46628 USA.

³ Present Address: Lamtec Corporation, 5010 River Road, Mount Bethel, PA 18343, USA.

fragments from these materials. Furthermore, these protocols have not yet been validated. It is critical to assess the applicability of techniques developed for quantification of MWCNTs for use with MWCNT nanocomposites, the capacity for various techniques to detect MWCNTs in polymer matrices at different MWCNT loadings, and the comparability among analytical techniques for analyzing MWCNTs in nanocomposite samples. In addition, measurements of the spatial distribution of MWCNTs in polymer nanocomposites are important both with regards to optimizing the manufacturing of these materials as well as the potential for MWCNT release. In a recent study, comparable results of the MWCNT spatial distribution were observed in nanocomposite materials at nominal mass loading concentrations of 1%, 4% and 5% using imaging X-ray photoelectron spectroscopy (XPS), scanning electron microscopy (SEM), and Raman imaging [27–29]. However, the capacity to assess the spatial distribution at lower concentrations, which are also highly relevant for MWCNT nanocomposite consumer products, was not determined.

In this study, the capacity for Raman spectroscopy, XPS, and SEM to characterize MWCNTs in nanocomposite samples at extremely low MWCNT concentration regime is evaluated. The nanocomposite samples were produced at National Institute of Standards and Technology (NIST) through industrially-relevant processes and spanned a concentration range of two orders of magnitude from a nominal mass fraction of MWCNT 0.01%–1% (referred to as simply “%” for the remainder of this work) [27,30,31]. The spatial analysis of MWCNTs was also assessed using samples at MWCNT concentrations of 0.3% and 1% with Raman and SEM imaging. Comparison of these different characterization techniques and their respective abilities to detect and locate MWCNTs in nanocomposite materials is detailed. The characterization protocols developed in this work can be utilized in future environmental and health studies involving low concentration of MWCNTs in released fragments from nanocomposites.

2. Experimental methods[†]

2.1. Nanocomposite sample preparation

MWCNT-epoxy nanocomposites were prepared at various MWCNT concentrations. Commercially available MWCNT (Graphistrength C100 (R&D), Batch 110314, Lot 005) were used as received from Arkema (King of Prussia, PA) and contained less than 12% catalyst as reported (aluminum oxide \leq 7% and iron oxide \leq 5%). The average nanotube size was determined by transmission electron microscopy (TEM) (average diameter = 31 nm \pm 7 nm, average length = 302 nm \pm 164 nm) [32] (unless otherwise noted, all uncertainties are one standard deviation taken from at least five measurements).

The matrix was comprised of a two-part epoxy/polyetherdiamine formulation. Bisphenol A diglycidyl ether (DGEBA, D.E.R. 332, Sigma Life Science, St. Louis, MO) was the epoxide monomer combined with two polyetherdiamine hardeners (Huntsman Jeffamines D-230 and D-2000 at a mass ratio of 9 to 1) to enhance epoxy toughness. Varying MWCNT mass fraction nanocomposites were prepared ranging from 0.01% to 1% (Fig. 1a). Visual inspection was used to optimize the mixing time, with more complete details regarding the preparation of the composite samples utilized in this study having been published previously [31,32]. For additional details regarding curing and MWCNT loading effects on dispersion, the reader is referred to prior studies [32, 33].

[†] Certain commercial product or equipment is described in this paper in order to specify adequately the experimental procedure. In no case does such identification imply recommendation or endorsement by the National Institute of Standards and Technology, nor does it imply that it is necessarily the best available for the purpose.

2.1.1. Bulk sample preparation

Nine pieces of bulk samples with a range of MWCNT mass loadings (0.01%, 0.05%, 0.10%, 0.20%, 0.30%, 0.40%, 0.50%, 0.75%, and 1%) were used for the Raman, SEM and XPS studies. The various formulations were poured into silicone molds and cured at 80 °C for 48 h. The lateral dimensions of the bulk samples were 25 mm by 75 mm and the thickness of each specimen varied as shown in Fig. 1a. These samples were prepared by grinding and subsequent sectioning as shown schematically in Fig. 1.

2.1.2. Thin film sample preparation

After macroscopic sectioning, thin films were subsequently prepared via an ultramicrotome (Leica Ultracut). Films with a thickness of 500 nm were sectioned and directly mounted on copper TEM grids. For direct comparison of the MWCNT heterogeneity within the polymer matrix, 0.30% and 1% MWCNT concentrations were imaged with Raman and SEM.

2.2. Raman spectroscopy

All Raman spectra were acquired under ambient conditions with a micro-Raman spectrometer (Renishaw InVia Raman system) equipped with three (514 nm, 633 nm and 785 nm) wavelength excitation lasers operating in 180° backscattering geometry. Spectra were collected through a 50 times magnification objective that focuses the excitation laser to an approximately 2 μ m diameter spot. Two gratings (1800 lines/mm and 1200 lines/mm) were in use for 633 nm/514 nm and 785 nm, respectively. A 1.25 cm charge-coupled device (CCD) detector was used to record the signal. Raman spectra on bulk samples were collected with all three-excitation wavelength with laser power of approximately 1 mW. Exposure time and accumulation numbers were tuned to obtain a spectrum with an acceptably high signal-to-noise ratio while minimizing acquisition time. Analysis was conducted on the MWCNT powder, neat polymer bulk samples, and MWCNT nanocomposite samples at various MWCNT loadings.

Raman mapping was performed on microtome samples with 0.30% and 1.00% MWCNT concentrations. For each sample, a large area Raman map was collected on an 80 μ m by 80 μ m area that spanned an entire window of the TEM grid with a raster step size of 4 μ m, and 60 s exposure time at each point (each area was scanned twice). Next, a smaller area within the larger region was selected for high resolution Raman mapping with a 0.75 μ m step size and 60 s exposure time at each point (each area was scanned twice). Maps were constructed with integrated area ratios of G' peak (2D) at approximately 2700 cm^{-1} to polymer peak at approximately 3100 cm^{-1} . Raman maps were created with a 514 nm excitation laser at which both peaks of interest (G' and the polymer peak) were able to be fully collected with a fixed grating measurement. The laser was maintained below 0.3 mW to avoid damaging the microtomed nanocomposite samples.

2.3. Scanning electron microscope and scanning transmission electron microscopy

SEM and scanning transmission electron microscopy (STEM in SEM) were performed with a focused ion beam (FIB) SEM (FEI Helios NanoLab 600, Hillsboro, OR) equipped with a retractable STEM detector. Before image acquisition, the NIST protocol²⁸ was followed to minimize the sources of electron-beam-induced contamination of the SEM itself using a low-energy oxygen plasma [34].

Secondary electron (SE) SEM images of the bulk specimens were acquired at 8 keV landing energy and 43 pA beam current. The TEM grids were used for SEM analysis using STEM following Raman analysis. Samples prepared for transmission electron microscopy analysis are sufficiently thin for STEM imaging in the SEM. Bright field (BF) STEM images of 500 nm thick samples were obtained at 30 keV electron landing energy and 1.4 nA beam current. Properly managing sample

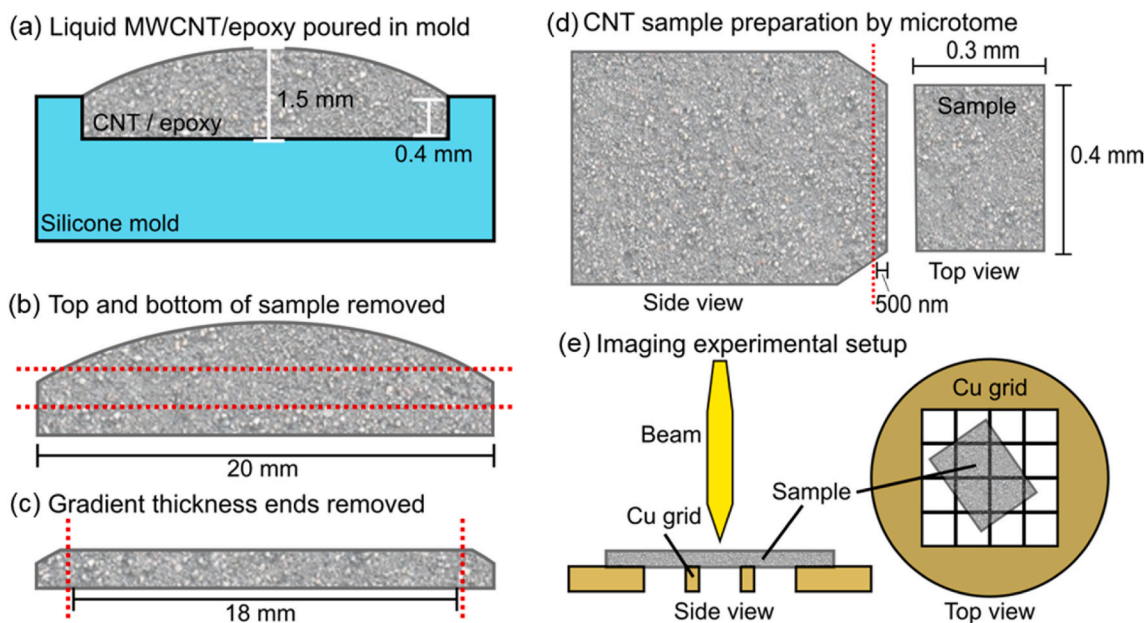


Fig. 1. Schematic of sample preparation of MWCNT nanocomposites. (a) Liquid MWCNT/epoxy mixture was poured into a silicone mold. Excess material was added to each cavity of the mold to prevent de-wetting. Significant curvature due to surface tension was observed on the top surface of each sample. (b–d) Subsequent sectioning of the cured MWCNT composite sample to a final size of 0.4 mm × 0.3 mm × 500 nm (standard deviation = 0.04 mm for larger dimensions and 20 nm for thickness dimension). Dashed lines indicate locations where material was removed, either by grinding (b) or direct sectioning (c and d). (e) Films (thickness = 500 nm) were prepared by microtoming and placed onto TEM grids for imaging by SEM and Raman. Both the side view (left) and top view (right) of the grid-mounted sample configuration are shown.

charging to take advantage of it is key to SEM imaging for identifying the amount, the distribution and the 3D structure of CNTs in epoxy. The samples proved to have sufficient conductivity to avoid charge accumulation that would prohibit SEM imaging. Excessive sample charging happened only with a pure epoxy sample, i.e., with no CNT. SE signal generation is a complex process, in which suitably controlled sample charging can be used to image CNTs at depths of couple of 100 nm deeper, into non-conductive epoxy[35]. The typical SE escape depth is a couple of nanometers for metals and up to about max. about 10 times as much for insulators. Thin Os conductive coating of bulk of samples made it possible to reveal areas where the CNTs were more or less evenly dispersed. Here also, managing of sample charging made this contrast viable for low magnification imaging. With uncoated samples, the effects of CNTs on sample charging, even in low (local) concentration, makes it possible to image CNTs at so high magnifications that the wall structure of MWCNTs and impurities can be revealed. The Supplementary Information Fig. 1 and 5 show evidence for this.

2.4. X-ray photoelectron spectroscopy (XPS)

Photoelectron spectra were acquired of bulk nanocomposite specimens on a spectrometer (Axis Ultra DLD, Kratos Analytical Ltd., Chestnut Ridge, NY). The polymer-rich surface layer of the nanocomposites was first removed with a milling tool (Leica TXP, Buffalo Grove, IL) as has been previously described [27] and loaded into the ultra-high vacuum (UHV) chamber ($P_{\text{base}} \approx 2.7 \cdot 10^{-7}$ Pa) to pump down overnight. Spectra were generated using monochromatic Al K_{α} X-rays operating at 104 W and emitted photoelectrons were collected along the surface normal in the absence of charge neutralization. Electrons were collected from an area defined by a hybrid lens and a slot aperture[36], and high resolution spectra were acquired at a pass energy of 40 eV. Wide range, survey spectra were also acquired, but at a pass energy 160 eV. Survey spectra were present to ensure that the expected signals were all present despite the charging. Survey spectra were also acquired in the absence of charging.

Samples spanning the full MWCNT sample loading range (0.01%–

1%) were analyzed by XPS. Spectra were acquired three to four times for each concentration of MWCNTs from spatially unique positions on the same specimen. Measurements were acquired every 0.1 eV with a dwell time of 0.3 s for ten or more sweeps. The lowest concentration samples (0.01% and 0.05%) were not measured within the same window for high resolution spectra due to a large degree of charging which yielded negligible counts.

Survey spectra were also acquired using charge neutralization to check for contaminants and catalyst contributions. For the 1.00% MWCNT composites, the survey spectra (not shown) appeared consistent with the epoxy composition with only carbon, oxygen and nitrogen signals present. For contaminants and catalysts, no other elements were detected and adventitious carbon could not be distinguished from the composite carbon signature if it was present.

3. Results and discussion

3.1. Raman, XPS, and SEM study on bulk samples with different MWCNT loading

3.1.1. Raman spectroscopy

Raman spectra of MWCNT powder and neat polymer were acquired using three different laser lines for use in comparing and extracting spectral information of the epoxy polymer and the MWCNTs, as can be seen in Fig. 2a and b, respectively. For each excitation line, the neat epoxy polymer is characterized by several sharp Raman features in the range of 500 cm^{-1} to 1700 cm^{-1} , as well as a set of peaks between 2500 cm^{-1} to 3200 cm^{-1} . Due to non-resonant Raman scattering, the positions of all polymer peaks are independent of laser energy. The Raman spectra for the raw MWCNT powder in the range of 500 cm^{-1} to 1700 cm^{-1} for each laser were dominated by D-band contributions (at approximately 1300 cm^{-1}), attributed to disorder induced by defects, and the G-band (at approximately 1600 cm^{-1}), due to the in-plane vibration of the graphite lattice[37,38]. In addition, the MWCNT powder exhibits the G' -band (2600 cm^{-1} to 2700 cm^{-1}), which is the overtone of the D-band.³⁰ The G-band position is independent of incident laser while

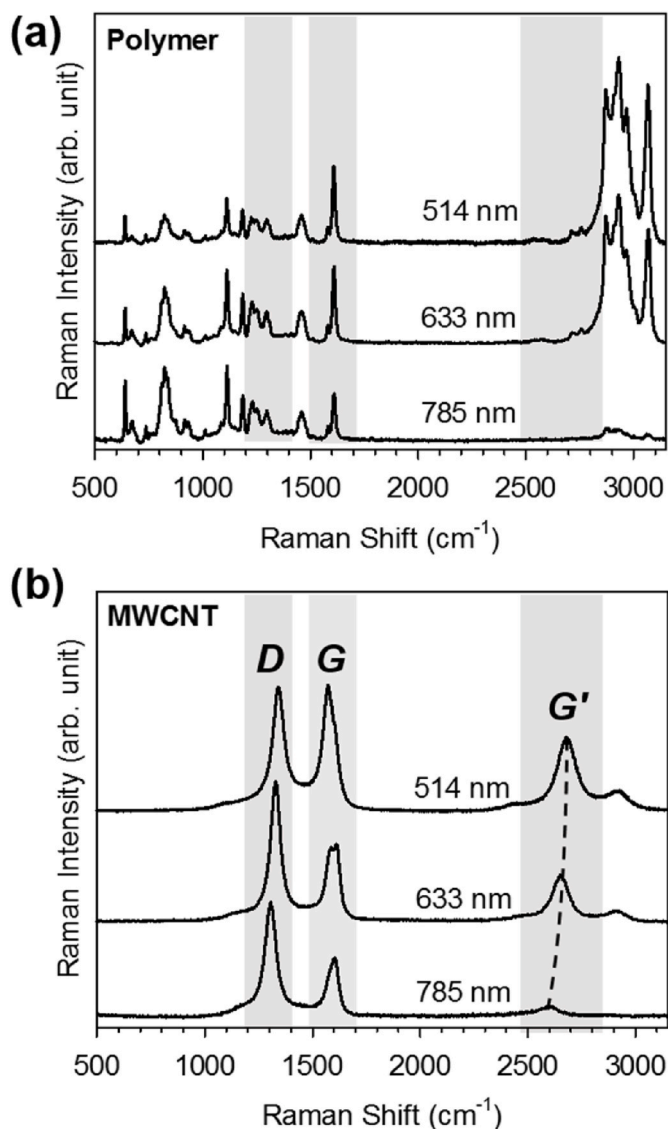


Fig. 2. Raman spectra of (a) neat polymer and (b) MWCNT powder with 514 nm, 633 nm, and 785 nm laser excitations. The spectra are offset for clarity. The D, G and G' peaks of MWCNT positions are highlighted in both figures. The dashed lines indicate the dispersive behavior of the G' peak.

the G'-band is dispersive to the excitation laser energy as indicated by the dashed lines in Fig. 2b [37]. Although it is not as readily apparent in Fig. 2b, the D-band position is also dispersive, though to a smaller degree.

Three commonly employed laser lines with wavelengths of 514 nm, 633 nm, and 785 nm were used to demonstrate the versatility of the Raman spectroscopy technique in characterizing MWCNT-epoxy based composites. Depending on the specific application, however, one laser line can be more advantageous over the other two. By comparing the spectra acquired at different laser energies seen in Fig. 2, one can observe that the spectra for the neat polymer is featureless around 2600 cm^{-1} , in contrast to the sharp G' peak in the MWCNT powder. Based on these results, the G' peak intensity was utilized to indicate the presence of MWCNT. The G' signal intensity from the 514 nm laser excitation was the most prominent of the three laser wavelengths in the 2500 cm^{-1} region. Therefore, the 514 nm laser was selected for Raman mapping purposes. All three spectra had higher intensities in the D and G peak regions than in the G' region. Although epoxy peaks are present at wavenumbers where D and G peaks appear, due to the distinct peak

shapes of the two materials, it is also possible to extract D or G peaks from the polymer features to detect the presence of MWCNTs. The 785 nm laser yielded the highest D/polymer peak intensity ratio and was selected to optimize detection measurements at extremely low MWCNT concentrations as will be discussed later in this paper.

The impact of MWCNT mass loading on the Raman spectra in bulk samples was evaluated using the 785 nm excitation. To average the effects from sample heterogeneity, 14 arbitrary, distinct positions were characterized and the averages from these spectra were plotted in Fig. 3a. The spectra were normalized to the polymer peak at 825 cm^{-1} so that the intensity evolution of the MWCNT peaks can be highlighted. The polymer peaks are clearly present in all spectra. Noticeably the D, G, and G' peak intensities gradually increased with increasing MWCNT concentration.

Of the three prominent MWCNT peaks, the D-band is the most intense feature when using 785 nm excitation, and therefore was chosen as the analysis target to assess the detection limit of Raman spectroscopy in the bulk samples with the lowest MWCNT loadings. Fig. 3b shows overlaid spectra from 1200 cm^{-1} to 1370 cm^{-1} of the neat polymer and the 0.01% MWCNT (the sample with the lowest MWCNT concentration analyzed in this study) composite and also the spectra after subtraction of the neat epoxy sample spectrum from that of the MWCNT nanocomposite sample. There is a clear difference between the neat polymer spectrum and the 1% nanocomposite spectrum; the difference matches the D-band features of MWCNTs[39]. This result demonstrates that Raman spectroscopy is capable of detecting the MWCNTs in bulk nanocomposites with mass loadings as low as 0.01%. Fisher et al. reported a Raman based, rapid, quantitative mapping technique of MWCNT in composites with detection capability as low as 2.40% MWCNT mass loading[25]. Findings in the present work suggest that, with careful spectra fitting and data analysis, the detection limit via Raman spectroscopy of MWCNT concentrations can reach as low as 0.01%.

Fig. 3c shows the trend of D peak intensity vs. MWCNT loading. Within the tested MWCNT loading range, higher MWCNT mass loadings correlate with higher D peak intensities. However, the relatively large standard deviations values, obtained from analyzing data taken from 14 arbitrary locations on each sample, indicate significant heterogeneity of the MWCNT distribution within the nanocomposite.

3.1.2. XPS

XPS spectra were acquired from MWCNT nanocomposites and are presented in Fig. 4. Consistent with previous studies[19,24,40,41], the prepared nanocomposites charged significantly when exposed to a flux of X-rays incident upon the surface due to the low conductivity associated with the epoxy rich nanocomposite regions. Fig. 4a demonstrates this by presenting the C (1s) regions for a subset of the nanocomposites measured. The C (1s) regions are dominated by the epoxy rich spectral feature at greater than or equal to 297 eV, significantly shifted from the typical aliphatic and aromatic carbon's binding energy range of 284.5 eV–285.0 eV, due to the positive charge at the surface. Furthermore, the peak maximum decreases in binding energy with increased nominal MWCNT concentration, an observation which previously has been attributed to the dissipation of charge facilitated at higher MWCNT concentration[27].

The y-scale of the C (1s) spectral regions are enhanced by two orders of magnitude around the region more commonly associated with aliphatic and aromatic carbon in Fig. 4b with Tougaard fits assigned to the lower binding energy tail of the charging epoxy rich feature. In the selected spectra, there is a spectral feature at a static location which has previously been attributed to MWCNT agglomerates within a composite by XPS imaging[27]. While this spectral feature is clearly present above the noise and increases with the nominal concentration of MWCNT added to the composite at concentrations of 0.10% and greater, a clearly resolved local maximum is consistently observed at approximately 284.5 eV only starting at concentrations of 0.5% and greater. To

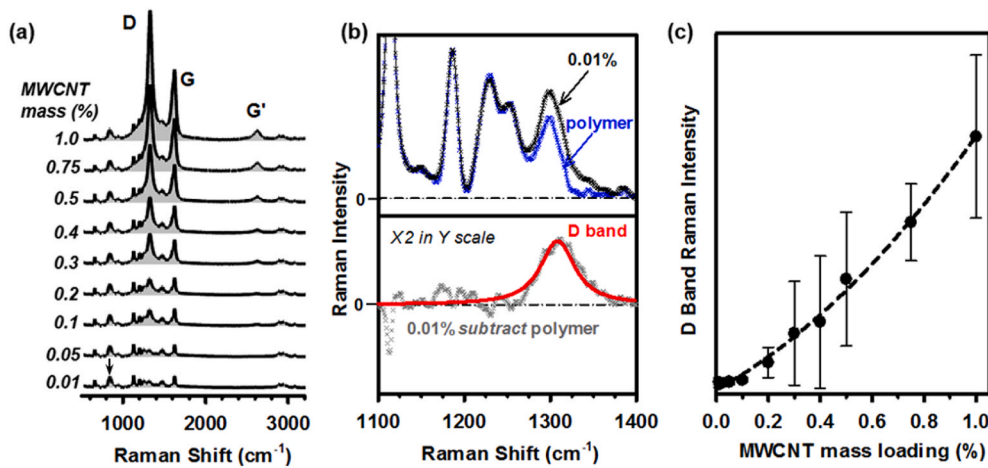


Fig. 3. (a) 785 nm laser excited Raman spectra of composites with different MWCNT mass loadings. All spectra were normalized to the polymer peak at approximately 825 cm^{-1} , indicated by the arrow, then offset for clarity. All spectra for (a) and (b) are the average of spectra collected from 14 random spots on each sample. (b) Enlarged 0.01% nanocomposite and polymer spectra containing the D-band region. Gray trace in the bottom panel is constructed by subtracting the polymer spectrum from that of nanocomposite. The leftover trace matched well with the D-band of MWCNT. (c) Maximum peak intensity at the D band position for each spectrum was plotted against MWCNT mass loading. The error bars are from the average of 14 spectra and 1 standard deviation, indicating the variability of MWCNT dispersion. The dashed line linking the points is only to more clearly show the trend and is not the result of fitting a specific

mathematical function.

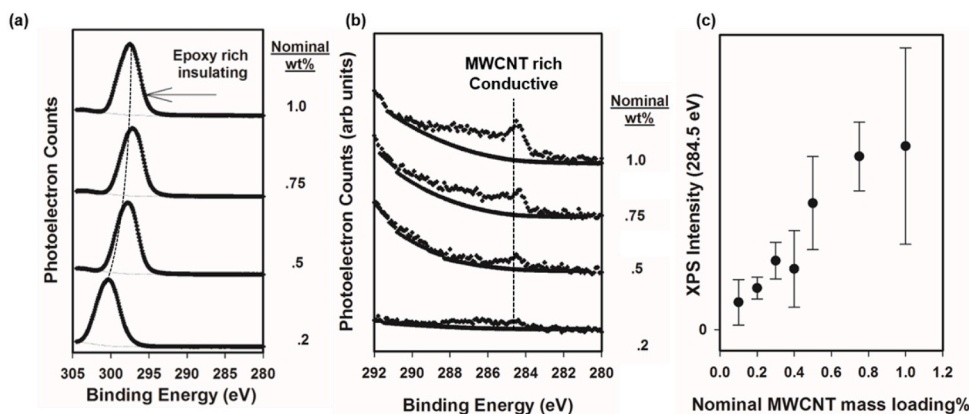


Fig. 4. (a) XP spectral profile of the C (1s) region is dominated by a charging feature shifted to higher binding energies. The peak position shifts to lower binding energy with increased nominal MWCNT concentration. (b) C (1s) region from (a) magnified approximately 100 times reveals an additional component at lower binding energies (approximately 284.5 eV) consistent with conductive carbon such as MWCNT. This conductive feature has been fit with a background, selected to mimic the lower binding energy side of the epoxy rich feature. (c) Plot of the background-subtracted XPS intensity versus nominal MWCNT loading at 284.5 eV . Data reflect an average of at least 3 measurements and 1 standard deviation.

demonstrate the change in this spectral feature with increased MWCNT loading, the average background-subtracted, intensity at 284.5 eV is plotted in Fig. 4c. The data and error bars are representative of the average plus or minus a standard deviation of 3 or 4 measurements at different points across a given sample to demonstrate the variability in

the dispersion of MWCNTs in each sample.

3.1.3. SEM and STEM

SE and STEM images were taken to assess the MWCNT distribution in the bulk epoxy composite sample. SE images of the bulk sample with

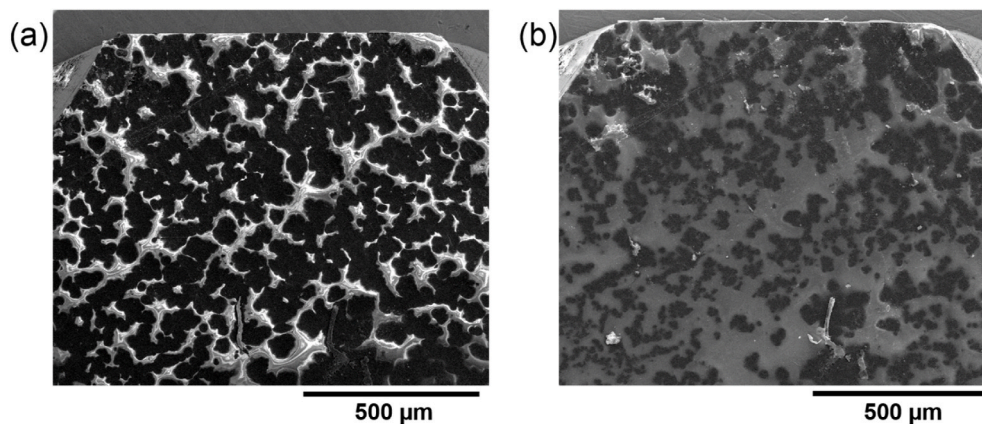


Fig. 5. SEM images of a bulk sample (0.30% MWCNT). The charge contrast reveals the MWCNT-rich (dark) and epoxy (bright) areas. (a) The bulk sample without any conductive layer. The charge build-up makes SE yields higher at epoxy-rich and lower at MWCNT-rich areas. (b) The bulk sample after 12 nm Os coating revealing the same information but with better spatial resolution and reportability.

0.30% MWCNT concentrations were taken before (Fig. 5a) and after (Fig. 5b) the application of a 12 nm osmium (Os) metal coating. In Fig. 5a, the charge contrast reveals the MWCNT- and epoxy-rich areas in a thick, partially conductive sample. Charge build-up yields brighter epoxy-rich patterns and darker MWCNT-rich areas, as CNTs limit sample charging and secondary electron yield[30]. Os coating allows for charging-artifact-free imaging (Fig. 5b). A several nm thin layer of Os metal can eliminate surface charging by keeping the sample surface at ground potential. However, it does not remove charging inside the sample, therefore some charge contrast within the bulk of the sample can still be observed in Fig. 5b [30]. The Os coated image reveals further fine details and structures on the top surface that cannot be observed in Fig. 5a. The main advantage of performing a SEM study on bulk samples without coating is that it can quickly produce a map indicating the MWCNT loading and distribution in MWCNT-nanocomposite samples [19].

3.2. Raman and SEM imaging: comparison and evaluation of homogeneity of MWCNT distribution

BF-STEM images of a 0.30% MWCNT concentration microtome sample confirms the existence of MWCNT in nanocomposite samples. Some areas in the nanocomposites have very high MWCNT concentrations (Fig. 6a) while other areas have medium to low MWCNT concentrations (Fig. 6b).

Although Raman spectra in Fig. 3 demonstrate the correlation between MWCNT Raman intensity versus mass loading and reveal the capacity of Raman analysis to identify MWCNTs in the lowest MWCNT concentration tested, the large variation indicated significant heterogeneity of the distribution of MWCNTs in the composites. To evaluate this distribution of MWCNTs in the nanocomposite, Raman and SEM imaging were conducted on the same sample and at the same location on microtomed samples with areas up to approximately 80 μm by 80 μm , with two commercially relevant MWCNT mass loadings of 0.30% and 1%. The results of the two techniques show remarkably well correlated MWCNT distributions, as shown in Fig. 7.

A large area survey scan was first conducted using Raman mapping and SEM on almost an entire window on the TEM grid of the 0.30% MWCNT nanocomposite film (Fig. 7). Fig. 7c shows an overlay of the Raman-mapping image (color) on top of the SEM image (black and white). The color contrast from blue to red indicates increasing MWCNT to polymer peak Raman intensity ratio and therefore increased local concentration of MWCNTs in the composite. Red color indicates a high concentration of MWCNTs, while blue indicates almost pure polymer in the mapping location. MWCNTs are randomly clustered into domains, or MWCNT hot spots, in the thin film. The MWCNT concentration in each domain varies significantly as indicated by the color. Within the surveyed imaging area, a smaller area containing domains of high and low concentrations of MWCNTs was chosen to analyze the inhomogeneity of

MWCNT distribution and resolve the fine structures of MWCNT domains (Fig. 7b). Fig. 7e reveals more detailed information regarding MWCNT domains that was not resolved in the larger area Raman mapping. The overlay of the SEM image and Raman map reveals that the resolved fine MWCNT hot spots were in excellent agreement with the observed MWCNT structure by SEM as shown in Fig. 7f. The neat polymer areas (less than 1 μm by 1 μm) among MWCNT hot spots are clearly resolved as seen in Fig. 7f. Significant overlap of Raman chemical imaging and electron microscopy data was also recently seen for other nanocarbon composites[28].

Three Raman spectra representing high MWCNT concentration domains, medium concentration MWCNT domains, and bare polymer areas from the 0.3% MWCNT nanocomposite films are presented in Fig. 8. To obtain these spectra, a linear cross line was taken from the Raman map in Fig. 7e. To better visualize the MWCNT concentration distribution, the same map was plotted in 3D form in Fig. 8a. Most of the MWCNTs are clustered in the lower left corner of the figure, as indicated by peaks with higher MWCNT to polymer intensity ratio. As shown in Fig. 8b, the intensity ratio across the MWCNT domain/neat polymer boundary showed significant variance. The blue dot indicates the highest ratio, and the corresponding spectrum was plotted in blue in Fig. 8c. Similarly, the pink and red dots indicate medium and low concentration of MWCNT, spectra of which are shown in Fig. 8c in matching colors. It is clear that the G' is absent when MWCNTs are not present, and as the MWCNT concentration increases, the G' intensity grows.

Similar Raman mapping and STEM and SE imaging were also conducted on a 1% MWCNT nanocomposite film (Fig. 9). Compared to the results from the 0.30% MWCNT composite film, both SEM and Raman images showed an increased total quantity of MWCNT domains and more high- MWCNT-density areas. Sample regions where the density of MWCNT were high overheated and small holes were created by the irradiating laser during Raman mapping. This was rarely observed in 0.30% sample using the same laser power and instrument settings. Both Raman and SEM confirmed the holes in the same location as indicated by the arrow in Fig. 9f. Overall, the overlay of the Raman and SEM images (Fig. 9c and f) show excellent agreement between the results of the two techniques.

3.3. Comparison of techniques and order of characterization methods

It is important to note that this study demonstrates a specific characterization order that needs to be followed when conducting and comparing Raman and SEM on the same sample. After characterization of the sample with Raman and then SEM, the same area of the sample was analyzed again with Raman using the same experiment conditions. Interestingly, the characteristic peaks from both MWCNTs and the epoxy polymer disappear. Instead, an intense fluorescence background was measured as can be seen in Fig. 10b. A large area Raman map was conducted on the same window as that in Fig. 7c. Although no peaks of

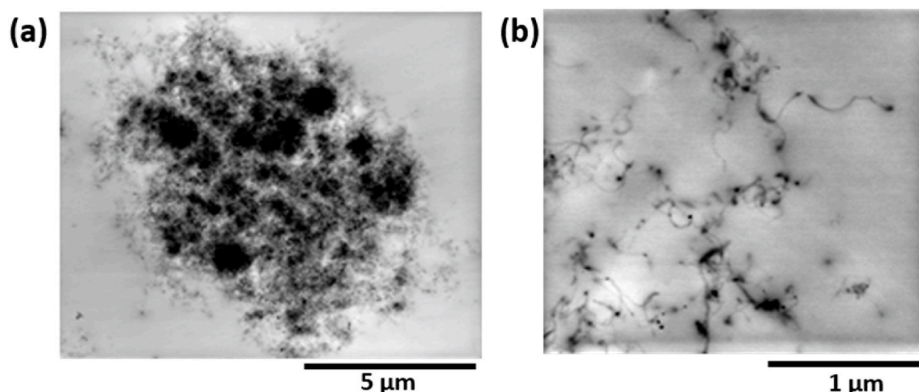


Fig. 6. Representative images from the same 0.30% MWCNT nanocomposite microtome sample showing both high (a) and low (b) MWCNT concentration areas.

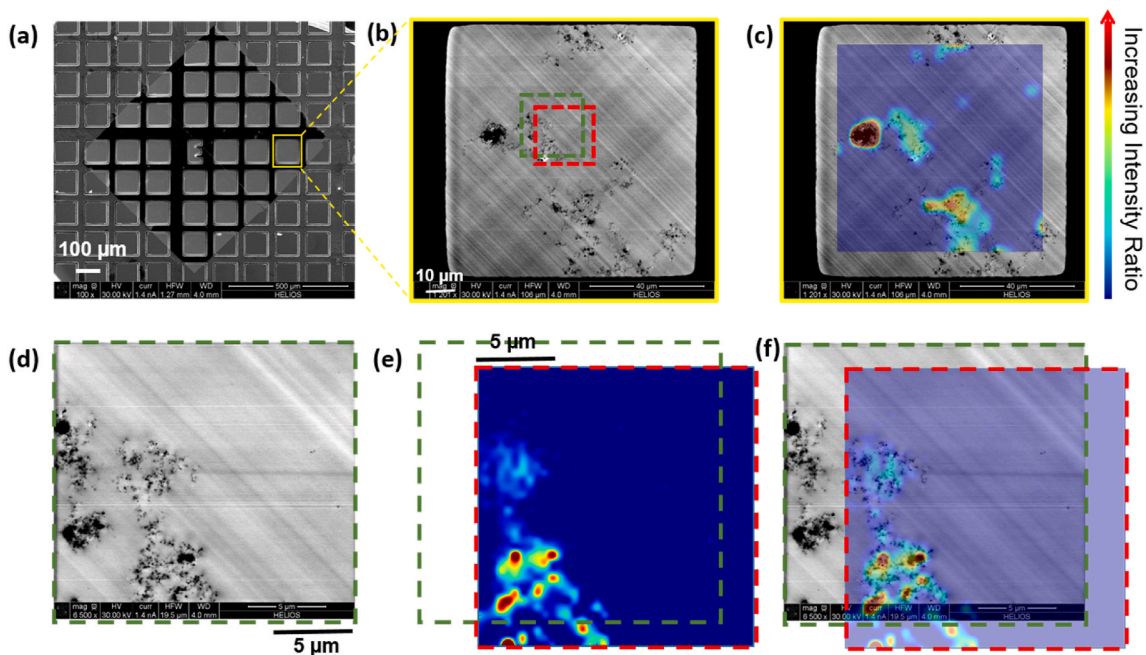


Fig. 7. A 500 nm thick nanocomposite film of 0.30% MWCNT on a TEM grid was used for both the SEM and Raman imaging. At each point of the Raman mapping, the integrated area ratio of G' to the polymer peak at 3067 cm^{-1} was plotted to yield the image of MWCNT concentration and distribution. (a) SEM image of large area containing multiple grid windows. (b) SEM image of window indicated by yellow box in (a), the striation is due to sample thickness variation caused by microtome blade. (c) Raman mapping of the same window in (b) overlaid on top of the SEM image. (d) SEM image of a smaller area in (b) indicated by green box. (e) Raman mapping of smaller area in (b) indicated by red box. (f) overlapping images of (d) and (e). (For interpretation of the references to color in this figure legend, the reader is referred to the Web version of this article.)

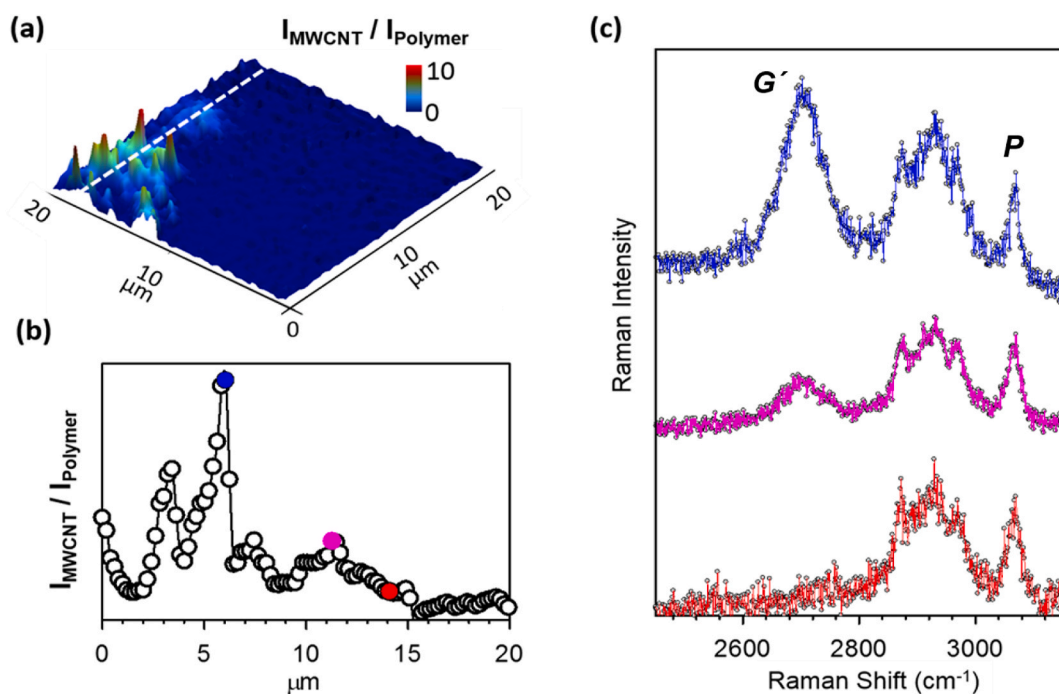


Fig. 8. (a) 3D form of Raman mapping image in Fig. 7e where the Z-intensity is a ratio of the integrated area of the MWCNT G' peak to that of the polymer peak at approximately 3067 cm^{-1} . (b) Line scan profile of the intensity ratio of MWCNT-to-polymer along the dashed white line in (a). (c) Raman spectra at three locations, indicated by colored dots in (b).

interest were observed, if a similar analysis method of plotting the intensity ratio of the fluorescence at the G' peak position to that at polymer peak position is applied, Fig. 10a is the resulting image. A clear square can be seen in the Raman mapping with lower $G'/$ polymer intensity

ratio. The square matches the position where the small area SEM was performed. The reason behind this observation is likely amorphous carbon deposition on the surface of the polymer composite caused by the electron beam during SEM imaging[42]. Both SEM and Raman are very

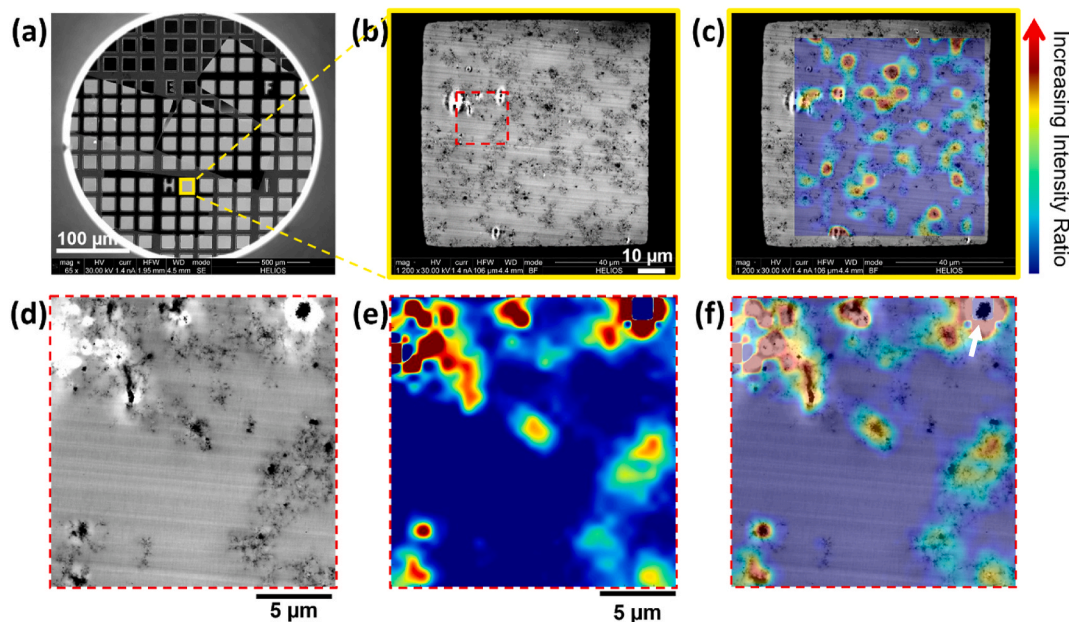


Fig. 9. 1% MWCNT polymer composite of 500 nm thickness film on a TEM grid imaged by SEM and Raman. At each point of the Raman mapping, the integrated area ratio of G' to the polymer peak at 3067 cm^{-1} is plotted to yield the image of MWCNT concentration and distribution. (a) SEM SE image of large area containing multiple windows. (b) BF-STEM image of single window indicated by yellow box in (a). (c) Raman mapping of the same window in (b) plotted on top of the SEM STEM image. (d) SEM image of smaller area in (b) indicated by red box. (e) Raman mapping of the same area as (d). (f) overlapping image of (d) and (e). Note this sample has 3x the MWCNT loading compared to Fig. 7. (For interpretation of the references to color in this figure legend, the reader is referred to the Web version of this article.)

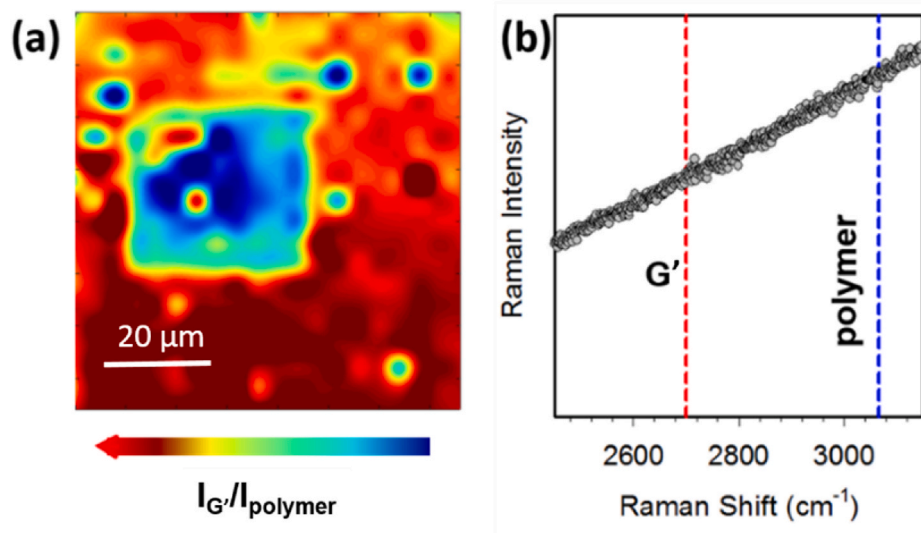


Fig. 10. (a) Raman re-map of the same area as in Fig. 7 (c) after SEM. Instead of distinct MWCNT and polymer peaks, a broad fluorescence band is observed in the Raman spectra. An example spectrum is shown in (b). The Raman map in (a) is constructed with the ratio of intensity at approximately 2700 cm^{-1} , the G' peak, to that at approximately 3067 cm^{-1} , the polymer peak.

common surface characterization techniques in the nanocomposite industry. Therefore, this observation suggests that when multiple techniques are involved, the order of characterization is critical for accurate characterization.

This study demonstrates that all three techniques, XPS, Raman and SEM, are capable of detecting MWCNTs in the nanocomposites and therefore can be used to cross-validate results. XPS is mostly limited by the sample size and the concentration of MWCNTs. While XPS is more surface sensitive, only bulk samples with a clearly resolved spectral feature are suitable for XPS analysis. Unlike XPS, Raman can be

performed on either bulk or thin film samples. In this study, Raman is capable of detecting the lowest MWCNT mass loading (0.01%). It should be noted that although industrial protocol was followed to produce the nanocomposites, MWCNTs are distributed in clusters regardless of loading concentration, and the localized concentrations of MWCNTs in the clusters made low concentration detection practical. Both XPS and Raman can provide information about the chemical composition of the sample, while SEM provides information about the structural composition. The tradeoff to sensitive Raman chemical imaging is a long acquisition time (hours). Indeed, XPS and Raman have both been

employed in the current study and previously to identify poor dispersions of MWCNTs in polymeric matrices by evaluating differences in conductivity between epoxy rich composite and MWCNT rich aggregates [27,43,44]. While unable to accurately quantify low concentrations of MWCNTs, the XPS is capable of noting the impact of increasing MWCNTs in these ‘epoxy rich’ regions of the composite as decreases in the magnitude of differential charging. In contrast, Raman is quite capable of detecting and quantifying much lower concentrations of MWCNTs in composites. Future studies could include the suit of measurement techniques spanning length scales; XPS and Raman imaging along with microscopy, to directly relate the conductivity changes to the dispersion/percolation of the MWCNTs in the epoxy matrix. In contrast, SEM can provide high spatially resolved images, down to the single MWCNT level (Supporting Information Figures S1 and S2) in minutes. However, SEM and STEM requires significant sample preparation involving sectioning and coating. A comparison of the three techniques is summarized in Supporting Information Table S1.

4. Conclusions

In summary, Raman, XPS and SEM techniques were leveraged to characterize MWCNT nanocomposite samples with nine different MWCNT percentages spanning from 0.01% to 1%, and two different thicknesses: the bulk sample and 500 nm thin films. In the bulk samples, Raman, XPS, and SEM results show general trends of increasing MWCNT features in the nanocomposites with higher MWCNT mass loadings. Raman was able to detect MWCNT signals from samples with the lowest MWCNT loading of 0.01%. Note that although low MWCNT concentrations were detected using Raman spectroscopy, this sensitivity is likely due to microscale clusters of MWCNTs. In other words, heterogeneities in the distribution of the MWCNTs enabled detection at very low nanoparticle concentrations. All three characterization techniques, Raman, SEM and XPS, indicated a significant inhomogeneous distribution of MWCNT in the nanocomposite. To evaluate the inhomogeneity of MWCNT distribution in the nanocomposites, Raman chemical imaging and SEM-STEM techniques were used to investigate 500 nm thick nanocomposite films with two different MWCNT percentages. The results from both techniques located MWCNT ‘hot spots’ or clusters in identical locations in these samples. The study also indicates a characterization order to be followed: Raman chemical imaging needs to be performed before SEM analysis to avoid sample damage or contamination.

Author Statement

Yanmei Piao: Investigation, Writing – Original Draft **Vipin N. Tondare:** Investigation **Chelsea S. Davis:** Investigation, Resources **Justin M. Gorham:** Investigation, Visualization **Elijah J. Petersen:** Conceptualization **Jeffrey W. Gilman:** Funding acquisition **Keana Scott:** Funding acquisition, Resources, Conceptualization **Andrés E. Vladár:** Investigation **Angela R. Hight Walker:** Project administration, Funding acquisition. All authors participated in Writing – Review and Editing.

Declaration of competing interest

The authors declare that they have no known competing financial interests or personal relationships that could have appeared to influence the work reported in this paper.

Acknowledgements

A part of this work was performed under the financial assistance award 60NANB15D238 from the U.S. Department of Commerce, National Institute of Standards and Technology.

Appendix A. Supplementary data

Supplementary data to this article can be found online at <https://doi.org/10.1016/j.compscitech.2021.108753>.

References

- [1] F. Hussain, Polymer-matrix nanocomposites, processing, manufacturing, and application: an overview, *J. Compos. Mater.* 40 (2006) 1511–1575, <https://doi.org/10.1177/0021998306067321>.
- [2] C.A. Cooper, D. Ravich, D. Lips, J. Mayer, H.D. Wagner, Distribution and alignment of carbon nanotubes and nanofibrils in a polymer matrix, *Compos. Sci. Technol.* 62 (2002) 1105–1112, [https://doi.org/10.1016/S0266-3538\(02\)00056-8](https://doi.org/10.1016/S0266-3538(02)00056-8).
- [3] K. Lau, M. Lu, Chun-ki Lam, H. Cheung, F.-L. Sheng, H.-L. Li, Thermal and mechanical properties of single-walled carbon nanotube bundle-reinforced epoxy nanocomposites: the role of solvent for nanotube dispersion, *Compos. Sci. Technol.* 65 (2005) 719–725, <https://doi.org/10.1016/j.compscitech.2004.10.005>.
- [4] D. Qian, E.C. Dickey, R. Andrews, T. Rantell, Load transfer and deformation mechanisms in carbon nanotube-polystyrene composites, *Appl. Phys. Lett.* 76 (2000) 2868, <https://doi.org/10.1063/1.126500>.
- [5] M.J. Biercuk, M.C. Llaguno, M. Radosavljevic, J.K. Hyun, A.T. Johnson, J. E. Fischer, Carbon nanotube composites for thermal management, *Appl. Phys. Lett.* 80 (2002) 2767–2769, <https://doi.org/10.1063/1.1469696>.
- [6] M. Cadek, J.N. Coleman, V. Barron, K. Hedicke, W.J. Blau, Morphological and mechanical properties of carbon-nanotube-reinforced semicrystalline and amorphous polymer composites, *Appl. Phys. Lett.* 81 (2002) 5123–5125, <https://doi.org/10.1063/1.1533118>.
- [7] M. Cadek, J.N. Coleman, K.P. Ryan, V. Nicolosi, G. Bister, A. Fonseca, J.B. Nagy, K. Szostak, F. Béguin, W.J. Blau, Reinforcement of polymers with carbon nanotubes: the role of nanotube surface area, *Nano Lett.* 4 (2004) 353–356, <https://doi.org/10.1021/nl035009o>.
- [8] R.H. Baughman, A.A. Zakhidov, W.A. de Heer, Carbon nanotubes—the route toward applications, *Science* 297 (80) (2002) 787–792, <https://doi.org/10.1126/science.1060928>.
- [9] H. Zhang, G. Zhang, M. Tang, L. Zhou, J. Li, X. Fan, X. Shi, J. Qin, Synergistic effect of carbon nanotube and graphene nanoplates on the mechanical, electrical and electromagnetic interference shielding properties of polymer composites and polymer composite foams, *Chem. Eng. J.* 353 (2018) 381–393, <https://doi.org/10.1016/j.cej.2018.07.144>.
- [10] J. Baur, E. Silverman, Challenges and opportunities in multifunctional nanocomposite structures for aerospace applications, *MRS Bull.* 32 (2007) 328–334, <https://doi.org/10.1557/mrs2007.231>.
- [11] J. Lee, S. Mahendra, P.J.J. Alvarez, Nanomaterials in the construction industry: a review of their applications and environmental health and safety considerations, *ACS Nano* 4 (2010) 3580–3590, <https://doi.org/10.1021/nn100866w>.
- [12] E.J. Petersen, S.A. Diamond, A.J. Kennedy, G.G. Goss, K. Ho, J. Lead, S.K. Hanna, N.B. Hartmann, K. Hund-Rinke, B. Mader, N. Manier, P. Pandard, E.R. Salinas, P. Sayre, Adapting OECD aquatic toxicity tests for use with manufactured nanomaterials: key issues and consensus recommendations, *Environ. Sci. Technol.* 49 (2015) 9532–9547, <https://doi.org/10.1021/acs.est.5b00997>.
- [13] H. Godwin, C. Nameth, D. Avery, L.L. Bergeson, D. Bernard, E. Beryt, W. Boyes, S. Brown, A.J. Clippinger, Y. Cohen, M. Doa, C.O. Hendren, P. Holden, K. Houck, A. B. Kane, F. Klaessig, T. Kodas, R. Landsiedel, I. Lynch, T. Malloy, M.B. Miller, J. Muller, G. Oberdorster, E.J. Petersen, R.C. Pleus, P. Sayre, V. Stone, K. M. Sullivan, J. Tentschert, P. Wallis, A.E. Nel, Nanomaterial categorization for assessing risk potential to facilitate regulatory decision-making, *ACS Nano* 9 (2015) 3409–3417, <https://doi.org/10.1021/acsnano.5b00941>.
- [14] K. Aschberger, H.J. Johnston, V. Stone, R.J. Aitken, S.M. Hankin, S.A.K. Peters, C. L. Tran, F.M. Christensen, Review of carbon nanotubes toxicity and exposure-appraisal of human health risk assessment based on open literature, *Crit. Rev. Toxicol.* 40 (2010) 759–790, <https://doi.org/10.3109/10408444.2010.506638>.
- [15] W. Wohlleben, M.W.W. Meier, S. Vogel, R. Landsiedel, G. Cox, S. Hirth, Z. Tomovic, Z. Tomovic, Elastic CNT-polyurethane nanocomposite: synthesis, performance and assessment of fragments released during use, *Nanoscale* 5 (2013) 369–380, <https://doi.org/10.1039/c2nr32711b>.
- [16] L. Schlagenhauf, T. Buerki-Thurnherr, Y.Y. Kuo, A. Wichser, F. Nüesch, P. Wick, J. Wang, Carbon nanotubes released from an epoxy-based nanocomposite: quantification and particle toxicity, *Environ. Sci. Technol.* 49 (2015) 10616–10623, <https://doi.org/10.1021/acs.est.5b02750>.
- [17] W. Wohlleben, N. Neubauer, Quantitative rates of release from weathered nanocomposites are determined across 5 orders of magnitude by the matrix, modulated by the embedded nanomaterial, *NanoImpact* 1 (2016) 39–45, <https://doi.org/10.1016/j.jimpact.2016.01.001>.
- [18] G.A. Sotiriou, D. Singh, F. Zhang, M.C.G. Chalbot, E. Spielman-Sun, L. Hoering, I. G. Kavouras, G.V. Lowry, W. Wohlleben, P. Demokritou, Thermal decomposition of nano-enabled thermoplastics: possible environmental health and safety implications, *J. Hazard Mater.* 305 (2016) 87–95, <https://doi.org/10.1016/j.jhazmat.2015.11.001>.
- [19] T. Nguyen, E.J. Petersen, B. Pellegrin, J.M. Gorham, T. Lam, M. Zhao, L. Sung, Impact of UV irradiation on multiwall carbon nanotubes in nanocomposites: formation of entangled surface layer and mechanisms of release resistance, *Carbon* N. Y. 116 (2017) 191–200, <https://doi.org/10.1016/j.carbon.2017.01.097>.
- [20] W. Wohlleben, C. Kingston, J. Carter, E. Sahle-Demessie, S. Vázquez-Campos, B. Acrey, C.Y. Chen, E. Walton, H. Egenolf, P. Müller, R. Zepp, NanoRelease, Pilot

- interlaboratory comparison of a weathering protocol applied to resilient and labile polymers with and without embedded carbon nanotubes, *Carbon N. Y.* 113 (2017) 346–360, <https://doi.org/10.1016/j.carbon.2016.11.011>.
- [21] D. Singh, G.A. Sotiriou, F. Zhang, J. Mead, D. Bello, W. Wohlleben, P. Demokritou, End-of-life thermal decomposition of nano-enabled polymers: effect of nanofiller loading and polymer matrix on by-products, *Environ. Sci. Nano.* 3 (2016) 1293–1305, <https://doi.org/10.1039/c6en00252h>.
- [22] P. Boonruksa, D. Bello, J. Zhang, J.A. Isaacs, J.L. Mead, S.R. Woskie, Characterization of potential exposures to nanoparticles and fibers during manufacturing and recycling of carbon nanotube reinforced polypropylene composites, *Ann. Occup. Hyg.* 60 (2015) 40–55, <https://doi.org/10.1093/annhyg/mev073>.
- [23] C. Kingston, R. Zepp, A. Andrady, D. Boverhof, R. Fehir, D. Hawkins, J. Roberts, P. Sayre, B. Shelton, Y. Sultan, V. Vejins, W. Wohlleben, Release characteristics of selected carbon nanotube polymer composites, *Carbon N. Y.* 68 (2014) 33–57, <https://doi.org/10.1016/j.carbon.2013.11.042>.
- [24] E.J. Petersen, D.X. Flores-Cervantes, T.D. Bucheli, L.C.C. Elliott, J.A. Fagan, A. Gogos, S. Hanna, R. Kägi, E. Mansfield, A.R.M. Bustos, D.L. Plata, V. Reipa, P. Westerhoff, M.R. Winchester, Quantification of carbon nanotubes in environmental matrices: current capabilities, case studies, and future prospects, *Environ. Sci. Technol.* 50 (2016) 4587–4605, <https://doi.org/10.1021/acs.est.5b05647>.
- [25] S.J. Fisher, M.S.P. Shaffer, Rapid quantitative mapping of multi-walled carbon nanotube concentration in nanocomposites, *Compos. Sci. Technol.* 160 (2018) 161–168, <https://doi.org/10.1016/j.compscitech.2018.03.010>.
- [26] L. Bokobza, Spectroscopic techniques for the characterization of polymer nanocomposites: a review, *Polymers* 10 (2018) 1–21, <https://doi.org/10.3390/polym10010007>.
- [27] J.M. Gorham, W.A. Osborn, J.W. Woodcock, K.C.K. Scott, J.M. Heddlestone, A. R. Hight Walker, J.W. Gilman, Detecting carbon in carbon: exploiting differential charging to obtain information on the chemical identity and spatial location of carbon nanotube aggregates in composites by imaging X-ray photoelectron spectroscopy, *Carbon N. Y.* 96 (2016) 1208–1216, <https://doi.org/10.1016/j.carbon.2015.10.073>.
- [28] A. McCreary, Q. An, A.M. Forster, K. Liu, S. He, C.W. Macosko, A. Stein, A.R. Hight Walker, Raman imaging of surface and sub-surface graphene oxide in fiber reinforced polymer nanocomposites, *Carbon N. Y.* 143 (2019) 793–801, <https://doi.org/10.1016/j.carbon.2018.11.014>.
- [29] D. Ryoo, J.Y. Kim, P.K. Duy, S.H. Cho, H. Chung, T.H. Yoon, Fast and non-destructive Raman spectroscopic determination of multi-walled carbon nanotube (MWCNT) contents in MWCNT/polydimethylsiloxane composites, *Analyst* 143 (2018) 4347–4353, <https://doi.org/10.1039/c8an00351c>.
- [30] A.E. Vladár, Strategies for scanning electron microscopy sample preparation and characterization of multiwall carbon nanotube polymer composites, *NIST - Spec. Publ.* 17 (1) (2015) 1–16, <https://doi.org/10.6028/NIST.SP.1200-17>, 1200.
- [31] C.S. Davis, J.W. Woodcock, J.W. Gilman, Preparation of Nanoscale Mutli-Walled Carbon Nanotube Dispersions in a Polyetheramine Epoxy for Eco-Toxicological Assessment, vol. 1200, *NIST Spec. Publ.*, 2015, <https://doi.org/10.6028/NIST.SP.1200-9>.
- [32] C.S. Davis, N.D. Orloff, J.W. Woodcock, C.J. Long, K.A. Twedt, B. Natarajan, J. E. Seppala, J.J. McClelland, J. Obrzut, J.A. Liddle, J.W. Gilman, Cure temperature influences composite electrical properties by carbon nanotube-rich domain formation, *Compos. Sci. Technol.* 133 (2016) 23–32, <https://doi.org/10.1016/j.compscitech.2016.07.012>.
- [33] B. Natarajan, N.D. Orloff, R. Ashkar, S. Doshi, K. Twedt, A. Krishnamurthy, C. S. Davis, A.M. Forster, E. Thostenson, J. Obrzut, R. Sharma, J.A. Liddle, Multiscale metrologies for process optimization of carbon nanotube polymer composites, *Carbon N. Y.* 108 (2016) 381–393, <https://doi.org/10.1016/j.carbon.2016.07.028>.
- [34] A.E. Vladár, K.P. Purushotham, M.T. Postek, Contamination specification for dimensional metrology SEMs, *Metrolog. Insp. Process Control Microolithogr.* XXII (6922) (2008) 692217, <https://doi.org/10.1117/12.774015>.
- [35] M. Zhao, B. Ming, J.W. Kim, L.J. Gibbons, X. Gu, T. Nguyen, C. Park, P.T. Lillehei, J.S. Villarrubia, A.E. Vladár, J. Alexander Liddle, Erratum, New insights into subsurface imaging of carbon nanotubes in polymer composites via scanning electron microscopy, *Nanotechnology* 26 (85703) (2015), <https://doi.org/10.1088/0957-4484/26/16/169601>. *Nanotechnology*. 26 (2015).
- [36] S.C. Barron, J.M. Gorham, M.P. Patel, M.L. Green, High-throughput measurements of thermo-chromic behavior in V1-xNb_xO₂ combinatorial thin film libraries, *ACS Comb. Sci.* 16 (2014) 526–534, <https://doi.org/10.1021/co500064p>.
- [37] M.S. Dresselhaus, G. Dresselhaus, R. Saito, A. Jorio, Raman spectroscopy of carbon nanotubes, *Phys. Rep.* 409 (2005) 47–99, <https://doi.org/10.1016/j.physrep.2004.10.006>.
- [38] L. Bokobza, J. Zhang, Raman spectroscopic characterization of multiwall carbon nanotubes and of composites, *Express Polym. Lett.* 6 (2012) 601–608, <https://doi.org/10.3144/expresspolymlett.2012.63>.
- [39] D. Kałuża, E. Jaworska, M. Mazur, K. Maksymiuk, A. Michalska, Multiwalled carbon nanotubes-poly(3-octylthiophene-2,5-diyl) nanocomposite transducer for ion-selective electrodes: Raman spectroscopy insight into the transducer/membrane interface, *Anal. Chem.* 91 (2019) 9010–9017, <https://doi.org/10.1021/acs.analchem.9b01286>.
- [40] J.M. Gorham, J.W. Woodcock, K.C. Scott, Challenges , Strategies and Opportunities for Measuring Carbon Nanotubes within a Polymer Composite by X-Ray Photoelectron Spectroscopy Challenges , Strategies and Opportunities for Measuring Carbon Nanotubes within a Polymer Composite by X-Ray Photoelect, *Spec. Publ.*, 2015, <https://doi.org/10.6028/NIST.SP.1200-10> (NIST SP) - 1200-10.
- [41] E.J. Petersen, T. Lam, J.M. Gorham, K.C. Scott, C.J. Long, D. Stanley, R. Sharma, J. Alexander Liddle, B. Pellegrin, T. Nguyen, J.A. Liddle, B. Pellegrin, T. Nguyen, J. Alexander Liddle, B. Pellegrin, T. Nguyen, J.A. Liddle, B. Pellegrin, T. Nguyen, Methods to assess the impact of UV irradiation on the surface chemistry and structure of multiwall carbon nanotube epoxy nanocomposites, *Carbon N. Y.* 69 (2014) 194–205, <https://doi.org/10.1016/j.carbon.2013.12.016>.
- [42] N.D. Bassim, B.T. De Gregorio, A.L.D. Kilcoyne, K. Scott, T. Chou, S. Wirick, G. Cody, R.M. Stroud, Minimizing damage during FIB sample preparation of soft materials, *J. Microsc.* 245 (2012) 288–301, <https://doi.org/10.1111/j.1365-2818.2011.03570.x>.
- [43] H.S. Kim, J.U. Jang, J. Yu, S.Y. Kim, Thermal conductivity of polymer composites based on the length of multi-walled carbon nanotubes, *Compos. B Eng.* 79 (2015) 505–512, <https://doi.org/10.1016/j.compositesb.2015.05.012>.
- [44] V. Tishkova, P.I. Raynal, P. Puech, A. Lonjon, M. Le Fournier, P. Demont, E. Flahaut, W. Bacsa, Electrical conductivity and Raman imaging of double wall carbon nanotubes in a polymer matrix, *Compos. Sci. Technol.* 71 (2011) 1326–1330, <https://doi.org/10.1016/j.compscitech.2011.05.001>.